Proceedings of the Pakistan Academy of Sciences: A Physical and Computational Sciences 63(1): 1-16 (2026)

ISSN (Print): 2518-4245; ISSN (Online): 2518-4253
http://doi.org/10.53560/PPASA(63-1)709

Pakistan Academy of Sciences

Research Article

Computational Approach to Unveil Mechanisms of Action of Sesquiterpene Glycosides from *Calendula officinalis* against Gastric Cancer

Hung Duc Nguyen*

Faculty of Biology, Thai Nguyen University of Education, Thai Nguyen, Vietnam

Abstract: Gastric cancer remains a major global health burden, and prognosis for advanced disease is frequently limited by late diagnosis and the toxicity of systemic chemotherapy. Mcl-1, an anti-apoptotic Bcl-2 family protein often overexpressed in gastric cancer, contributes to apoptosis evasion and treatment resistance, supporting its relevance as a therapeutic target. In this study, sesquiterpene glycosides from *Calendula officinalis* were evaluated as Mcl-1 (PDB: 6QFQ)-directed ligands using an integrated in silico workflow, with Etoposide as a reference. Docking identified CPD2 as the top-ranked compound (-10.75 kcal/mol), exceeding Etoposide (-9.80 kcal/mol), with a binding mode dominated by nonpolar contacts within the pocket and hydrogen-bond assignment to Arg263 and Leu267. During 100 ns molecular dynamics simulations, both complexes remained stable; CPD2 showed a RMSD values predominantly between 0.11-0.15 nm after equilibration and lower compactness/solvent-exposure trends (Rg 1.42-1.44 nm; SASA 82-88 nm²) relative to the Etoposide complex. MM/GBSA predicted a favorable association for both ligands, yielding comparable ΔTOTAL values (-28.72 ± 4.45 kcal/mol for CPD2; -29.80 ± 10.53 kcal/mol for Etoposide). ADMET prediction indicated high intestinal absorption for CPD2 (94.482%) despite low water solubility (-5.034 log mol/L), and DFT suggested greater electronic pliability for CPD2 (ΔE = 5.2502 eV) than Etoposide (ΔE = 11.1496 eV). Overall, CPD2 emerges as a prioritized computational hit for structure-guided optimization, and subsequent biochemical and cellular validation is expected to clarify its translational potential.

Keywords: Anti-apoptosis, *Calendula officinalis*, Gastric Cancer, In Silico, Mcl-1, Sesquiterpene Glycosides.

1. INTRODUCTION

Cancer remains a significant global health threat, with an estimated 20 million new cases and over 10 million deaths annually. Both incidence and mortality rates are rising due to factors like population aging, lifestyle risk factors, and disparities in healthcare access [1]. Forecasts further anticipate a marked expansion in annual incidence by 2050 (approximately 30.5 to 35 million cases), representing about a 77% increase relative to 2022, mainly attributable to demographic growth, longer life expectancy, and development-associated risks such as tobacco use, alcohol consumption, and obesity [2]. Gastric cancer remains the world's fifth most common cancer and the fifth leading cause of cancer-related deaths globally. Although treatment options have advanced, including surgery, systemic chemotherapy, and molecularly targeted approaches, outcomes for advanced gastric cancer remain unfavorable because many cases are detected late and exhibit rapid dissemination, leaving few curative opportunities, and median survival is commonly below one year [3, 4]. Standard management typically combines chemotherapy with surgery and/or radiotherapy according to disease stage, tumor location, and patient condition [5]. However, cytotoxic chemotherapy frequently damages proliferative normal tissues, causing fatigue, gastrointestinal toxicity, mucositis, and alopecia, and may also induce myelosuppression, neuropathy, appetite loss, and organ toxicities; effects are drug-dependent and are mainly managed with supportive care [6]. This toxicity and tolerability profile supports continued investigation of safer adjunctive or alternative strategies,

Received: January 2026; Revised: February 2026; Accepted: March 2026
* Corresponding Author: Hung Duc Nguyen <hungnd@tnue.edu.vn>

including plant-derived bioactive candidates for gastric cancer management.

Mcl-1 (Myeloid cell leukemia-1) is a key anti-apoptotic protein often overexpressed in gastric cancer, promoting tumor growth, invasion, and resistance to chemotherapy by blocking programmed cell death. Its high expression indicates a worse prognosis for patients. It is associated with advanced stages, making it a significant target for novel therapies, especially when combined with standard treatments to enhance effectiveness [7-9]. Systematic investigation has identified several natural products traditionally used for gastric disorders that exhibit potential Mcl-1-modulating activity in gastric cancer cells. These compounds can induce apoptosis by downregulating the anti-apoptotic protein Mcl-1 or shifting its splicing towards the pro-apoptotic variant [10, 11]. The use of *Calendula officinalis* L. (known as Jin Zhan Ju) in Traditional Chinese Medicine is primarily for topical applications to promote circulation and healthy skin. However, in Western and folk herbal medicine traditions, it is often used internally to treat various gastric diseases such as gastritis, stomach ulcers, and inflammatory bowel conditions [12]. This ethnopharmacological background provides a rationale for focusing on characteristic secondary metabolites of *C. officinalis*, particularly constituents with reported anticancer potential. Sesquiterpene glycosides are natural compounds found in plants, formed by a sesquiterpene linked to one or more sugar units, which confer water solubility. They are known for diverse biological activities, including anti-inflammatory, enzyme inhibition, and anticancer activities. Previous study indicates that sesquiterpene glycosides isolated from *C. officinalis* show significant promise for treating gastric cancer [13]. Despite these observations, the specific target-level basis underlying the reported anticancer effects, especially with respect to apoptosis-regulatory proteins, has not been clearly delineated. Accordingly, the mechanistic link between sesquiterpene glycosides and Mcl-1-mediated apoptotic control remains incompletely defined at the molecular level. To address this gap, a multi-computational approach was implemented to map binding propensity and stability, integrating structure-based docking with time-resolved molecular dynamics, MM/GBSA, in silico ADMET profiling, and DFT calculations. This combined framework enables comparative candidate prioritization and provides a rational basis for subsequent experimental verification and structure-guided lead refinement in gastric cancer drug development.

2. MATERIALS AND METHODS

2.1. Data Collection

These selected sesquiterpene glycosides, including α-Elemol 11-*O*-β-D-fucopyranoside 2′-*O*-angelate ester (CPD1), β-Eudesmol-β-D-fucopyranoside-2’-*O*-angelate (CPD2), officinoside D (CPD3), have molecular formulas of $C_{26}H_{42}O_6$, $C_{26}H_{42}O_6$, $C_{27}H_{44}O_6$, respectively, with molecular weights of 450.2981, 450.2981, 464.3138 *m/z*. Etoposide, possessing a molecular formula of $C_{29}H_{32}O_{13}$ and a molecular weight of 588.1843 *m/z*, was chosen as the positive control (Figure 1).

2.2. Molecular Docking Analysis

Three-dimensional structures of the selected ligands and Etoposide were generated in PDB format using BIOVIA Discovery Studio Visualizer. During ligand preparation, polar hydrogen atoms were added, Gasteiger partial charges were assigned, and torsional degrees of freedom were retained by treating rotatable bonds as flexible. The crystallographic coordinates of the anti-apoptotic protein Mcl-1 (PDB ID: 6QFQ) were retrieved from the RCSB Protein Data Bank [14].

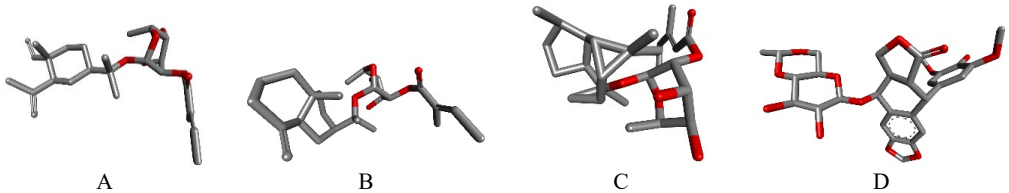

Fig. 1. 3D Structures of selected ligands. (A) CPD1, (B) CPD2, (C) CPD3, (D) Etoposide.

Because Mcl-1 is closely associated with apoptosis resistance in gastric cancer, this target was selected to evaluate the disease relevance of the investigated sesquiterpene glycosides. Docking calculations were performed with AutoDock Tools using a cubic search space defined by 60 grid points along each Cartesian axis (x, y, z) at a spacing of 0.375 Å, with the grid center positioned at x = 3.934 Å, y = -18.343 Å, and z = 18.680 Å to cover the binding region. Conformational exploration and pose prioritization were conducted using the Lamarckian genetic algorithm, enabling identification of energetically favorable binding orientations and consistent interaction patterns. The highest-scoring protein-ligand complex was subsequently examined in Discovery Studio Client 2024, and its interaction profile was assessed in parallel with the docking pose of Etoposide within the same Mcl-1 structure to delineate overlapping or divergent binding characteristics.

2.3. Molecular Dynamics Simulations

Molecular dynamics simulations were conducted to evaluate the time-dependent stability of the docked Mcl-1-ligand complex based on the Mcl-1 crystal structure (PDB ID: 6QFQ). This analysis was performed to further examine the behavior of the prioritized complexes in a gastric cancer-relevant Mcl-1 targeting context. Simulations were executed in GROMACS 2024.4 employing the CHARMM36 force field over a 100 ns trajectory [15]. Protein preprocessing involved reconstruction of missing atoms and residues using Swiss-PdbViewer [16], whereas CHARMM-compatible ligand topology and parameter files were generated via SwissParam [17]. The assembled complex was placed in a triclinic periodic simulation cell, solvated with SPC water, and supplemented with NaCl to achieve 0.15 M ionic strength while ensuring overall electroneutrality. To alleviate steric clashes and unfavorable contacts, steepest-descent energy minimization was applied for 50,000 steps. The equilibration stage consisted of 100 ps under the NVT ensemble at 300 K followed by 100 ps under the NPT ensemble at 1 bar. System stability prior to production was assessed by monitoring temperature, pressure, and potential energy, which reached stable behavior before the 100 ns production run. To ensure stable numerical integration with a 2 fs time step, covalent bonds involving hydrogen atoms were constrained using the LINCS algorithm. The production stage comprised a single 100 ns run for each complex with a 2 fs integration step, and coordinate frames were saved every 10 ps for subsequent analysis. Trajectory-derived descriptors were obtained in Grace, including root mean square deviation (RMSD), root mean square fluctuation (RMSF), radius of gyration (Rg), solvent-accessible surface area (SASA), and number of hydrogen bonds (Hbonds). Conformational agreement among representative structures was additionally assessed in UCSF Chimera (v1.13.3) via coordinate superposition to compare characteristic states across the simulations [18].

2.4. Molecular Mechanics Generalised Born Surface Area (MM/GBSA) Analysis

Binding free-energy calculations for the CPD2-6QFQ and Etoposide-6QFQ complexes were performed using the gmx_MMPBSA workflow in conjunction with the CHARMM36 parameter set. This step was used to refine ligand prioritization against the gastric cancer-relevant target Mcl-1. The polar solvation contribution was computed with a generalized Born implicit-solvent approach, while the non-polar solvation component was estimated from solvent-accessible surface area. Energetic components were extracted from the molecular dynamics trajectories by analyzing 125 evenly distributed snapshots, sampled at 80 ps intervals over an 80 ns evaluation period spanning 20-100 ns. Mean values obtained from this snapshot ensemble enabled a direct comparison of ligand-protein interaction energetics and facilitated interpretation of relative binding propensity and complex persistence within the simulated timeframe [19].

2.5. Assay Protocol for ADMET Prediction

Early evaluation of absorption, distribution, metabolism, excretion, and toxicity (ADMET) properties is essential for identifying prospective pharmacokinetic constraints and safety concerns, thereby guiding compound selection and mitigating late-stage attrition. In the present study, this analysis supported the early selection of compounds with potential suitability for gastric cancer-related drug development. Thus, the pkCSM web platform was used to estimate the ADMET profiles of CPD2 and Etoposide computationally. pkCSM utilizes graph-based molecular signatures to predict descriptors linked to absorption, distribution, metabolism,

excretion, and toxicity, facilitating a systematic comparison of developability-related attributes between the examined compounds [20].

2.6. Quantum Chemistry Computation Using the Density Functional Theory (DFT) Method

Geometric optimization of CPD2 and Etoposide was carried out using the ORCA quantum-chemistry package (v6.1.0). Initial molecular geometries were assembled in Avogadro, and molecular-orbital inspection, along with associated electronic analyses, was performed in IboView (v20211019). Density functional theory computations were executed with the B3LYP exchange-correlation functional and the 6-31G(d,p) basis set to obtain electronic wavefunctions at the optimized minima. This level of theory was selected because it provides a practical balance between computational cost and reliability for geometry optimization and frontier-orbital analysis of small organic molecules. However, because these calculations were performed in the gas phase, solvent effects and dispersion-related contributions were not explicitly accounted for, and the resulting electronic descriptors may overestimate molecular pliability relative to an implicitly solvated aqueous environment. Based on the converged structures, frontier-orbital energies (HOMO and LUMO) were extracted, and the energy gap (ΔE) was determined. Conceptual DFT indices, chemical potential (μ), electronegativity (χ), global hardness (η), softness (σ), and electrophilicity index (ω), were subsequently derived using a Koopmans-type approximation, enabling interpretation of electronic structure features and reactivity trends for the investigated molecules [21-23].

3. RESULTS AND DISCUSSION

3.1. Molecular Docking Analysis

Molecular docking enables *in silico* estimation of preferred ligand orientations within a protein cavity and provides a comparative proxy for binding propensity through scoring functions that approximate noncovalent stabilization. Contemporary structure-based discovery workflows commonly interpret docking outputs by integrating energetic ranking with recurrence of pocket-defining residues and interaction classes (hydrogen bonding, hydrophobic, and van der Waals interactions) [24]. These interaction modes contribute in distinct yet cooperative ways: hydrogen bonding supports directional polar anchoring, whereas hydrophobic and dispersion-driven contacts enhance geometric complementarity and thermodynamic stabilization of protein-ligand assemblies [25].

As summarized in Table 1, CPD2 produced the most favorable docking score (-10.75 kcal/mol), followed by CPD3 (-10.64 kcal/mol) and CPD1 (-10.51 kcal/mol). Because Mcl-1 is implicated in apoptosis resistance in gastric cancer, this favorable docking profile suggests that CPD2 may have potential relevance as a gastric cancer-oriented Mcl-1 modulator. Each of these three candidates exceeded the reference Etoposide (-9.80 kcal/mol) under the same docking workflow, indicating higher

Table 1. The interactions between the docked ligands and the protein 6QFQ.

Docked ligands	Binding energy (kcal/mol)	Hydrogen bond interaction	Van der Waals interaction	Hydrophobic interaction
CPD1	-10.51	Arg263, Leu267	Ala227, Val253, Phe254, Thr266, Leu290	Phe228, Met231, Leu235, Leu246, Val249, Met250, Phe270, Val274, Leu267
CPD2	-10.75	Arg263, Leu267	Phe254, Thr266, Gly271, Val274, Leu290	Phe228, Met231, Leu235, Leu246, Val249, Met250, Val253, Leu267, Phe270
CPD3	-10.64	Met250, Leu267	His224, Val249, Val253, Phe254, Gly271	Ala227, Phe228, Met231, Leu235, Leu246, Val274, Leu290, Ile294
Etoposide	-9.80	Arg263, Thr266, Leu267	Leu235, Val249, Val253, Phe254, Gly262, Gly271, Val274, Ile294	His224, Ala227, Phe228, Met231, Leu246, Met250, Arg263, Thr266, Phe270, Leu290

predicted affinity within the scoring function used. Because docking scores represent an approximate ranking derived from the balance of modeled non-covalent terms, subsequent validation with dynamic sampling and more rigorous free-energy estimation remains advisable when advancing to mechanistic interpretation [26]. CPD2 engaged a compact interaction constellation dominated by hydrophobic and aromatic residues (Phe228, Met231, Val249, Met250, Val253, Ile267, Phe270), supplemented by Arg263 and Gly271 as annotated active-site participants. Hydrogen-bond contacts were assigned to Arg263 and Leu267, suggesting polar anchoring at the Arg263 side chain together with backbone-mediated polar complementarity in the vicinity of residue 267. Van der Waals contributions were reported for Phe254, Thr266, Gly271, Val274, and Leu290, consistent with close-range packing at the cavity periphery. The hydrophobic interaction list for CPD2 (Phe228, Met231, Leu235, Leu246, Val249, Met250, Val253, Leu267, Phe270) indicates extensive nonpolar burial, which is commonly associated with stabilization of ligand poses through desolvation and dispersion complementarity in aqueous environments (Figure 2A) [27, 28].

Relative to CPD2, CPD1 displayed a closely related contact pattern but incorporated Ala227 among the annotated active-site residues (Ala227, Phe228, Met231, Val249, Met250, Val253, Arg263, Ile267, Phe270). Hydrogen bonds were likewise assigned to Arg263 and Leu267, implying a conserved polar-recognition element shared with CPD2. The van der Waals interaction set for CPD1 (Ala227, Val253, Phe254, Thr266, Leu290) and the hydrophobic set (Phe228, Met231, Leu235, Leu246, Val249, Met250, Phe270, Val274, Leu267) support an interaction model in which tight packing against Phe228/Phe270 and multiple aliphatic side chains dominates, while Arg263 contributes a recurrent directional component [29].

CPD3 differed by recruiting His224 as an additional pocket contact (His224, Ala227, Phe228, Met231, Val249, Met250, Val253, Ile267, Gly271), and its hydrogen-bond annotations shifted to Met250 and Leu267 rather than Arg263. This pattern is consistent with an alternative polar-anchoring scheme centered on Met250 (likely via backbone participation, given the limited hydrogen-bonding capacity of the Met side chain) while maintaining

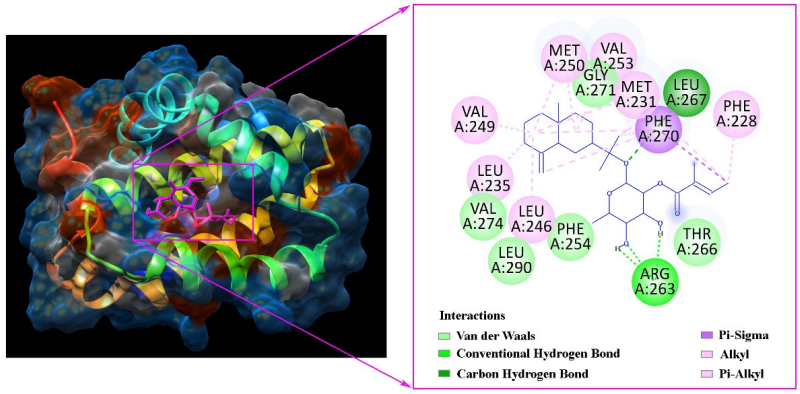

A

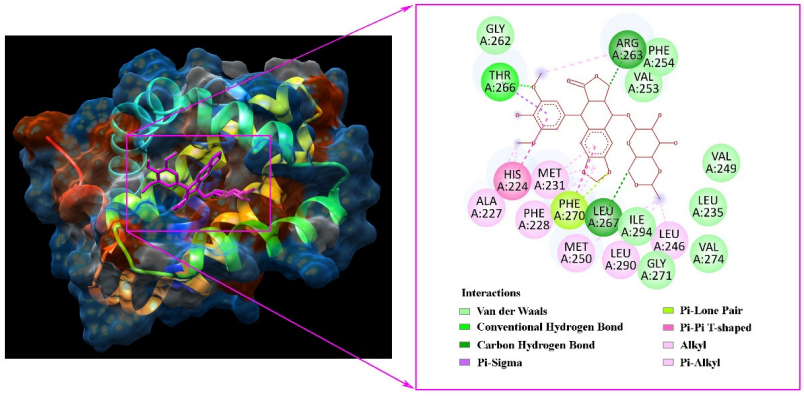

B

Fig. 2. Molecular docking model and 2D interaction diagram of CPD2 (A) and Etoposide (B) with 6QFQ protein.

residue-267 involvement. CPD3 also exhibited van der Waals interactions with His224, Val249, Val253, Phe254, and Gly271, and hydrophobic contacts extending toward Ile294 (Ala227, Phe228, Met231, Leu235, Leu246, Val274, Leu290, Ile294), implying a slightly reoriented pose that samples an adjacent nonpolar subregion of the binding cavity. Etoposide occupied an overlapping core region with broader residue coverage (His224, Ala227, Phe228, Met231, Val249, Met250, Val253, Gly262, Arg263, Ile267, Phe270, Gly271). Hydrogen bonds were assigned to Arg263, Thr266, and Leu267, indicating a triad of polar contacts that includes Thr266, a residue also present in the van der Waals or active-site lists of the CPD series. The van der Waals set for Etoposide (Leu235, Val249, Val253, Phe254, Gly262, Gly271, Val274, Ile294). Hydrophobic interactions (His224, Ala227, Phe228, Met231, Leu246, Met250, Arg263, Thr266, Phe270, Leu290) suggest simultaneous utilization of both aromatic/hydrophobic packing and multiple polar-capable residues, albeit with a less favorable docking score than CPD1-CPD3 (Figure 2B).

Across all four ligands, repeated engagement of Phe228, Met231, Val249, Met250, Val253, Leu267, and Phe270 supports the presence of a conserved recognition nucleus dominated by aromatic and aliphatic side chains, a physicochemical context in which dispersion and hydrophobic effects frequently contribute substantially to pose stabilization [30]. Differences in annotated hydrogen-bond partners imply ligand-dependent anchoring preferences that may alter residence within local minima of the docking energy landscape and could affect stability once receptor and solvent flexibility are represented explicitly. For this reason, pose refinement using interactions and follow-on molecular dynamics, with endpoint or more rigorous free-energy methods, can improve confidence beyond docking rank-order alone.

3.2. Molecular Dynamics Simulations

Molecular dynamics (MD) simulations are an established computational approach for resolving time-dependent atomic motions in molecular systems. By integrating the equations of motion under defined force fields and solvent conditions, MD yields trajectories that capture conformational fluctuations and interaction patterns at the atomic level. This capability supports mechanistic interrogation of phenomena that remain challenging to access experimentally, including protein folding pathways, ligand recognition and retention, allosteric rearrangements, and structure-property relationships in materials. Consequently, MD has become a core component of modern workflows in drug discovery, molecular chemistry, and materials engineering [31]. A 100 ns molecular dynamics protocol was carried out for the CPD2-6QFQ and Etoposide-6QFQ systems, and trajectory-derived conformational ensembles were examined through backbone RMSD, residue RMSF, radius of gyration (Rg), solvent-accessible surface area (SASA), and hydrogen-bond monitoring to characterize structural deviation, compactness, surface exposure, and polar-contact persistence [32]. The CPD2-6QFQ complex exhibited total and potential energies of -220,699 kJ/mol and -274,708 kJ/mol, respectively, whereas the corresponding values for Etoposide-6QFQ were -220,400 kJ/mol and -274,358 kJ/mol. Temperature regulation maintained the simulations at 300 K.

The time-resolved structural descriptors differentiate the dynamical signatures of the CPD2-6QFQ and Etoposide-6QFQ complexes over the 100 ns trajectory. In the backbone RMSD profiles, CPD2-6QFQ shows an early relaxation phase followed by a comparatively narrow fluctuation envelope, with most frames distributed around 0.11-0.15 nm and without a pronounced long-term drift (Figure 3A). This stable dynamic behavior is consistent with the prioritization of CPD2 for further investigation against the gastric cancer-relevant target Mcl-1. By contrast, the Etoposide-6QFQ trace stabilizes at a higher RMSD level and displays broader variability, frequently occupying 0.16-0.22 nm, with intermittent excursions toward 0.24-0.27 nm during the early segment and again in the late trajectory. Such persistent separation between RMSD bands is commonly interpreted as a higher-amplitude conformational response of the protein-ligand assembly rather than purely stochastic thermal noise, particularly when sustained over tens of nanoseconds [33].

For residue-wise flexibility, the analysis is restricted to Asp172-Val321, which contains the principal recognition corridor reported by docking (including His224, Ala227, Phe228, Met231, Val249-Val253, Arg263, Thr266, Leu267, Phe270, and Val274). Within this segment, both complexes

exhibit low-amplitude fluctuations, remaining largely below 0.10 nm across most positions (Figure 3B). RMSF represents the standard deviation of positional fluctuations around an average structure after optional fitting, and low RMSF values are generally consistent with retention of local secondary-structure order. A modest upward shift of the Etoposide trace relative to CPD2 is apparent across much of this interval, suggesting slightly increased local mobility of the groove region when Etoposide is bound, even though the most prominent RMSF maxima in the full-length profile occur outside the Asp172-Val321 window. This pattern supports a model in which CPD2 stabilizes the binding groove segment more effectively, whereas Etoposide is associated with a somewhat more compliant local environment.

Compactness and solvent exposure metrics exhibit coherent trends with RMSD/RMSF. The radius of gyration (Rg) for CPD2-6QFQ remains lower overall and more uniform, with most values clustered around 1.42-1.44 nm after initial equilibration (Figure 3C). Etoposide-6QFQ shows a higher central tendency and broader excursions, occupying 1.44-1.48 nm for extended intervals and briefly sampling still more expanded conformations early in the run. In parallel, SASA values for CPD2-6QFQ concentrate primarily around 82-88 nm², while Etoposide-6QFQ remains shifted upward (commonly 88-95 nm²) and more variable (Figure 3D). Elevated Rg together with persistently higher SASA is consistent with increased solvent exposure and a less compact protein ensemble, which can reflect cavity breathing motions or partial loosening of tertiary packing in response to ligand accommodation.

The hydrogen-bond time series reveals a mechanistic distinction in the mode of stabilizing interaction. Etoposide-6QFQ sustains a denser hydrogen-bonding pattern, particularly within the first 20 ns, where 1-3 hydrogen bonds dominate with occasional peaks reaching 4 (Figure 3E). Beyond

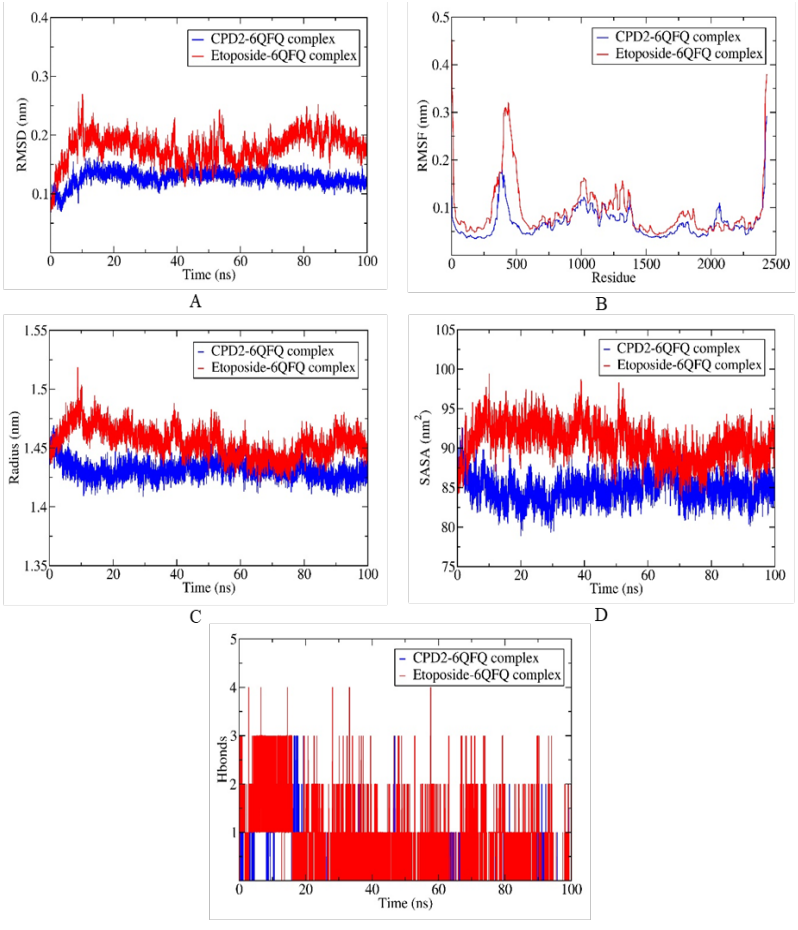

Fig. 3. Results of MD simulation for the bindings of CPD2 (blue) and Etoposide (red) with 6QFQ protein. (A) RMSD, (B) RMSF, (C) Rg, (D) SASA, (E) Hbonds.

this period, the Etoposide complex continues to display recurrent hydrogen-bond events (typically 0-1, punctuated by frequent short-lived rises to 2-3 and occasional spikes). In contrast, CPD2-6QFQ presents sparse hydrogen bonding for most of the trajectory, with prolonged intervals at zero and only intermittent episodes reaching 1; higher counts appear mainly as short bursts (including transient peaks up to 3) rather than a sustained network. High-occupancy hydrogen bonding is often associated with increased interaction specificity. It can support pose retention, yet the current comparison indicates that hydrogen-bond abundance alone does not necessarily correlate with reduced global backbone deviation, underscoring that nonpolar packing, dispersion stabilization, and collective protein motions may dominate the net dynamical response. Despite its lower hydrogen-bond persistence, CPD2 maintained lower RMSD, Rg, and SASA values throughout the simulation, indicating that its stability was not dependent on a dense hydrogen-bond network. Instead, the CPD2-6QFQ complex appears to be stabilized predominantly by hydrophobic enclosure and van der Waals complementarity, consistent with the docking interaction pattern.

Taken together, the combined metrics indicate that CPD2-6QFQ adopts a more compact and conformationally restrained ensemble (lower RMSD, lower Rg, reduced SASA) despite limited hydrogen-bond persistence, consistent with stabilization driven predominantly by hydrophobic enclosure and close-range packing. Etoposide-6QFQ, while exhibiting more frequent hydrogen-bond formation, shows larger-amplitude structural fluctuations and higher solvent exposure, suggesting greater conformational plasticity of the protein in the bound state. Within contemporary simulation-based screening pipelines, such a profile supports prioritization of CPD2 for subsequent energetic refinement while retaining Etoposide as a comparative reference due to its distinct polar-contact signature.

3.3. Free Binding Energy (MM/GBSA) Analysis

MM/GBSA is an end-state free-energy scheme that combines molecular-mechanics interaction terms (van der Waals and Coulombic electrostatics) with an implicit-solvent treatment in which the polar solvation contribution is approximated by a generalized Born (GB) model. In contrast, the nonpolar term is often associated with solvent-accessible surface area (SASA). In routine applications, configurational entropy is frequently excluded because of cost and methodological variability; consequently, MM/GBSA is typically interpreted as a comparative ranking metric whose outcomes depend on sampling quality and model choices such as dielectric settings and solvation parametrization [34, 35].

As reported in Table 2, both CPD2-6QFQ and Etoposide-6QFQ display favorable mean total binding free energies (ΔTOTAL), equal to -28.72 ± 4.45 kcal/mol and -29.80 ± 10.53 kcal/mol, respectively. Given the role of Mcl-1 in gastric cancer cell survival, these energetics support the relevance of CPD2 as a computationally promising ligand in this disease setting. The slightly more negative mean for Etoposide suggests a marginally stronger association within the same MM/GBSA protocol; however, the substantially larger dispersion for Etoposide across components (notably ΔVDWAALS and ΔEEL) indicates greater energetic heterogeneity among sampled configurations, which can arise from broader pose

Table 2. Free energy of binding obtained using MMGBSA calculations.

Energy component	Average (kcal/mol)		Standard deviation	
	CPD2-6QFQ	Etoposide-6QFQ	CPD2-6QFQ	Etoposide-6QFQ
ΔVDWAΔALS	-34.96	-41.35	4.29	9.50
ΔEEL	-2.39	-20.21	4.87	9.38
ΔEGB	12.82	37.27	4.90	8.14
ΔESURF	-4.19	-5.50	0.54	1.02
ΔGGAS	-37.35	-61.57	5.50	13.89
ΔGSOLV	8.63	31.77	4.93	7.97
ΔTOTAL	**-28.72**	**-29.80**	**4.45**	**10.53**

microstate diversity or larger amplitude fluctuations of interfacial contacts.

Energy decomposition indicates distinct driving forces. For CPD2-6QFQ, the gas-phase term is moderately favorable (ΔGGAS = -37.35 ± 5.50 kcal/mol) and is dominated by dispersion stabilization (ΔVDWAALS = -34.96 ± 4.29 kcal/mol), whereas Coulombic electrostatics contribute only weakly (ΔEEL = -2.39 ± 4.87 kcal/mol). This interaction gain is counterbalanced by a comparatively small net solvation penalty (ΔGSOLV = 8.63 ± 4.93 kcal/mol), arising primarily from the polar desolvation contribution (ΔEGB = 12.82 ± 4.90 kcal/mol) and partially compensated by a favorable nonpolar surface term (ΔESURF = -4.19 ± 0.54 kcal/mol). Such a profile is consistent with a binding mode that relies mainly on close-range packing and hydrophobic/van der Waals complementarity, while incurring a limited polar desolvation cost.

In contrast, Etoposide-6QFQ exhibits substantially stronger gas-phase stabilization (ΔGGAS = -61.57 ± 13.89 kcal/mol), reflecting both enhanced van der Waals attraction (ΔVDWAALS = -41.35 ± 9.50 kcal/mol) and markedly favorable electrostatics (ΔEEL = -20.21 ± 9.38 kcal/mol). These gains are opposed by a much larger solvation penalty (ΔGSOLV = 31.77 ± 7.97 kcal/mol), dominated by the GB polar component (ΔEGB = 37.27 ± 8.14 kcal/mol) with a modest compensatory nonpolar term (ΔESURF = -5.50 ± 1.02 kcal/mol). The near-cancellation between stronger vacuum interactions and amplified polar desolvation rationalizes why ΔTOTAL remains close to that of CPD2 despite the more attractive ΔGGAS. This energetic balance is frequently observed for ligands with pronounced electrostatic engagement, where favorable Coulombic contacts often coincide with increased desolvation costs in implicit-solvent end-state formalisms [36].

Overall, the MM/GBSA results indicate that both ligands are predicted to bind favorably, with Etoposide showing a slightly more negative mean ΔTOTAL but substantially higher variability. At the same time, CPD2 presents a more compact energetic distribution and a binding signature primarily governed by dispersion with a minor desolvation penalty. Given the known sensitivity of end-state estimates to sampling and parameterization, the close ΔTOTAL values (within the observed standard deviations) support a conservative interpretation in which CPD2 and Etoposide exhibit broadly comparable MM/GBSA binding tendencies under the present setup, and additional validation through extended sampling and/or entropy-aware refinements would improve confidence in fine rank distinctions.

3.4. ADMET Prediction Analysis

In silico ADMET screening is commonly used as an early developability filter because it summarizes absorption, distribution, metabolism, excretion, and safety-relevant liabilities before resource-intensive experimental campaigns. Such predictions are most reliable for comparative triage within a consistent workflow and should be interpreted alongside assay confirmation, given model dependence on training data, chemical domain, and endpoint definitions [37]. Table 3 summarizes the in silico ADMET outputs for CPD2 and Etoposide, providing a comparative overview of predicted absorption, distribution, metabolism, excretion, and toxicity parameters used to support early developability assessment.

- **Absorption:** The absorption panel differentiates CPD2 and Etoposide primarily through solubility-permeability balance. CPD2 shows lower predicted aqueous solubility (-5.034 log mol/L) than Etoposide (-3.487 log mol/L), suggesting a larger dissolution constraint for CPD2 despite favorable membrane transport metrics. In parallel, CPD2 shows higher predicted Caco-2 permeability (1.144 vs 0.403 log Papp) and higher predicted human intestinal absorption (94.482% vs 75.614%), consistent with a stronger epithelial transport propensity upon solubilization. Caco-2 permeability is widely used as a surrogate of intestinal transcellular permeation, although assay and model variability can influence absolute interpretation [38]. Skin permeability predictions are more negative for CPD2 (-3.327 log Kp) than for Etoposide (-2.735 log Kp), indicating lower modeled transdermal permeation for CPD2 under the same estimator. Both compounds are classified as P-glycoprotein (P-gp) substrates and as P-gp I/II inhibitors, a combination that may complicate exposure prediction because efflux liability and transporter inhibition can modulate net absorption and drug-drug interaction risk depending on co-administered substrates and inhibitors.

Table 3. Predicted ADMET properties of CPD2 and Etoposide.

ADMET properties	Unit	CPD2	Etoposide
Water Solubility	(Log mol/L)	-5.034	-3.487
Caco2 permeability	(Log Papp in 10-6 cm/s)	1.144	0.403
Intestinal absorption (Human)	(% Absorbed)	94.482	75.614
Skin permeability	(Log Kp)	-3.327	-2.735
P-glycoprotein substrate	Yes/No	Yes	Yes
P-glycoprotein I inhibitor	Yes/No	Yes	Yes
P-glycoprotein II inhibitor	Yes/No	Yes	Yes
VDss	(Log L/kg)	-0.301	-0.218
Fraction unbound (human)	(Fu)	0.05	0.038
BBB permeability	(Log BB)	-0.018	-1.567
CNS permeability	(Log PS)	-2.529	-4.115
CYP2D6 substrate	Yes/No	No	No
CYP3A4 substrate	Yes/No	Yes	Yes
CYP1A2 inhibitor	Yes/No	No	No
CYP2C19 inhibitor	Yes/No	No	No
CYP2C9 inhibitor	Yes/No	No	No
CYP2D6 inhibitor	Yes/No	No	No
CYP3A4 inhibitor	Yes/No	No	No
Total clearance	(Log ml/min/kg)	0.96	-0.068
Renal OCT2 substrate	Yes/No	Yes	No
AMES toxicity	Yes/No	No	No
Max. tolerated dose (human)	(Log mg/kg/day)	-0.21	0.171
hERG I inhibitor	Yes/No	No	No
hERG II inhibitor	Yes/No	No	No
Oral rat acute toxicity (LD50)	(mol/kg)	2.637	3.25
Oral rat chronic toxicity (LOAEL)	(Log mg/kg_bw/day)	2.36	2.429
Hepatotoxicity	Yes/No	No	No
Skin sensation	Yes/No	No	No
Tetrahymena pyriformis toxicity	(Log ug/L)	0.31	0.285
Minnow toxicity	(Log mM)	0.644	2.217

- **Distribution:** Distribution descriptors indicate broadly similar systemic disposition with notable divergence in CNS-related indices. VDss values are comparably low (-0.301 log L/kg for CPD2; -0.218 log L/kg for Etoposide), while the predicted unbound fraction is slightly higher for CPD2 (Fu = 0.05) than for Etoposide (Fu = 0.038), implying a modestly larger free circulating pool for CPD2. CNS exposure surrogates separate the compounds: CPD2 shows higher predicted BBB permeability (logBB = -0.018) than Etoposide (logBB = -1.567), and likewise higher predicted CNS permeability (logPS = -2.529 vs -4.115). Contemporary BBB modeling emphasizes that logBB/logPS indices primarily support comparative ranking rather than definitive brain exposure prediction, especially when transporter effects (e.g., P-gp at the BBB) are plausible [39].

- **Metabolism:** The metabolic liability panel indicates convergent biotransformation routing. Both CPD2 and Etoposide are predicted to be CYP3A4 substrates and non-substrates for CYP2D6, suggesting a predominant dependence on CYP3A-mediated oxidative metabolism rather than CYP2D6 turnover. No inhibition alerts are reported for CYP1A2, CYP2C19, CYP2C9, CYP2D6, or CYP3A4 for either compound, which reduces, without eliminating, concerns about CYP-mediated perpetrator drug-drug interactions in this prediction

set. Because CYP3A4 contributes substantially to clinical drug clearance, substrate classification remains relevant for victim interaction potential in the presence of potent CYP3A inhibitors or inducers [40].

- **Excretion:** Clearance predictions diverge markedly: CPD2 shows a higher predicted total clearance (0.96 log mL/min/kg) than Etoposide (-0.068 log mL/min/kg), consistent with faster modeled systemic elimination for CPD2 within the same framework. Renal OCT2 substrate classification is positive for CPD2 and negative for Etoposide, implicating a potential role of cation-transport pathways for CPD2 renal handling and transporter-mediated variability. OCT2 (often in functional interplay with MATE transporters) is recognized as an essential determinant of renal secretion and transporter-based interactions for susceptible substrates [41].

- **Toxicity:** Both compounds are predicted as AMES-negative, indicating no modeled bacterial mutagenicity signal, and both are classified as non-inhibitors for hERG I and hERG II in the provided output, which is generally interpreted as a lower predicted risk for hERG-associated cardiotoxicity within the limitations of in silico classifiers. Modern computational toxicology highlights that mutagenicity and hERG endpoints benefit from confirmation using orthogonal experimental assays because false negatives remain possible outside model applicability domains [42]. Additional toxicity-related outputs indicate no predicted hepatotoxicity or skin sensitization for either ligand. The maximum tolerated dose (human) is lower for CPD2 (-0.21 log mg/kg/day) than for Etoposide (0.171 log mg/kg/day). Acute oral rat LD50 is 2.637 mol/kg (CPD2) versus 3.25 mol/kg (Etoposide), while chronic oral rat LOAEL values are similar (2.36 vs 2.429 log mg/kg_bw/day). Aquatic toxicity proxies differ by endpoint: *T. pyriformis* toxicity is 0.31 (CPD2) versus 0.285 log µg/L (Etoposide), and minnow toxicity is 0.644 (CPD2) versus 2.217 log mM (Etoposide), indicating non-uniform environmental toxicity trends across organisms and units [43].

Overall, CPD2 combines high predicted intestinal absorption and higher modeled epithelial permeability with substantially poorer predicted solubility, indicating that formulation or solubility optimization could be a limiting consideration if empirical solubility confirms the trend. From a gastric cancer drug-development perspective, this profile suggests that CPD2 has encouraging absorption-related properties, although solubility may require further optimization. Etoposide presents comparatively better solubility but lower predicted intestinal absorption and permeability indices. Both ligands share P-gp substrate and inhibitor classifications, which may influence oral exposure and interaction risk in transporter-sensitive contexts. Distribution predictions indicate markedly reduced CNS exposure for Etoposide relative to CPD2 (logBB/logPS), while metabolism predictions suggest shared CYP3A4 substrate dependence with no predicted CYP inhibition flags. Clearance and renal transporter outputs further separate the profiles, with CPD2 showing higher predicted clearance and a positive OCT2-substrate classification, consistent with a potentially greater contribution of renal transporter processes to variability.

3.5. Quantum Chemistry Computation Using the DFT Method

DFT-derived frontier orbital energies and global conceptual-DFT descriptors were used to contextualize the electronic response characteristics of CPD2 relative to Etoposide (Table 4). In the frontier-orbital framework, a higher (less negative) HOMO energy is commonly associated with increased electron-donating propensity, whereas a lower LUMO energy is often linked to greater electron-accepting capability; the HOMO-LUMO separation (ΔE) is frequently interpreted as an index of electronic adaptability, where smaller gaps suggest easier polarization and charge redistribution under perturbation [44]. Table 4 presents the DFT-derived frontier orbital energies (EHOMO, ELUMO, and ΔE) together with key conceptual-DFT reactivity descriptors (μ, χ, η, σ, and ω) for CPD2 and Etoposide to support a comparative assessment of their electronic structure and global reactivity profiles.

CPD2 exhibits EHOMO = -3.1299 eV, substantially higher than that of Etoposide (-8.3206 eV), supporting a comparatively stronger donor character for CPD2 under the same computational protocol. In the acceptor channel, CPD2 also exhibits a lower ELUMO (2.1203 eV) than

Table 4. Quantum descriptors of CPD2 and Etoposide.

Molecule	EHOMO (eV)	ELUMO (eV)	ΔE (eV)	μ (eV)	χ (eV)	η (eV)	σ (eV^{-1})	ω (eV)
CPD2	-3.1299	2.1203	5.2502	-0.5048	0.5048	2.6251	0.3809	0.0485
Etoposide	-8.3206	2.8290	11.1496	-2.7458	2.7458	5.5748	0.1794	0.6762

EHOMO (eV): highest occupied molecular orbitals; **ELUMO (eV)**: lowest unoccupied molecular orbitals; **ΔE (eV)**: energy gap; **μ (eV)**: chemical potential; **χ (eV)**: electronegativity; **η (eV)**: hardness; **σ (eV^{-1})**: softness; **ω (eV)**: electrophilicity index.

Etoposide (2.8290 eV), indicating a more accessible accepting orbital. Consistent with these trends, CPD2 shows a markedly smaller ΔE (5.2502 eV) than Etoposide (11.1496 eV), suggesting that CPD2 is electronically more pliable, while Etoposide is characterized by a more rigid electronic structure with higher kinetic stability in the conceptual-DFT sense (Figure 4A, B) [45].

Global descriptors reinforce this separation. The chemical potential is less harmful for CPD2 (μ = -0.5048 eV) than for Etoposide (μ = -2.7458 eV), while electronegativity follows the inverse relation (χ = 0.5048 eV for CPD2; 2.7458 eV for Etoposide), indicating a stronger electron-attracting tendency for Etoposide. Hardness-softness behavior is consistent with the gap ordering: CPD2 exhibits lower hardness (η = 2.6251 eV) and higher softness (σ = 0.3809 eV^{-1}), whereas Etoposide shows higher hardness (η = 5.5748 eV) and lower softness (σ = 0.1794 eV^{-1}), implying greater resistance to electron-density deformation for Etoposide.

The electrophilicity index further differentiates charge-acceptance propensity at the global level. CPD2 presents a low ω value (0.0485 eV), while Etoposide displays a notably higher ω (0.6762 eV). Using the conceptual-DFT definition ($\omega = \mu^2/2\eta$) and commonly cited interpretive scales, both values fall within the marginal electrophile range, yet Etoposide retains a substantially stronger electrophilic signature than CPD2. This electronic profile is compatible with an interaction model in which CPD2 is more polarizable and donation-prone, whereas Etoposide expresses comparatively stronger electron-withdrawing character despite its larger orbital gap and higher hardness [46, 47]. These conceptual-DFT trends should be interpreted with caution because the calculations were performed in the gas phase; therefore, the apparent electronic pliability of CPD2 may be somewhat overestimated relative to a solvated environment. However, the smaller HOMO-LUMO gap and higher softness of CPD2 still suggest greater electronic adaptability, which may facilitate more efficient adjustment to

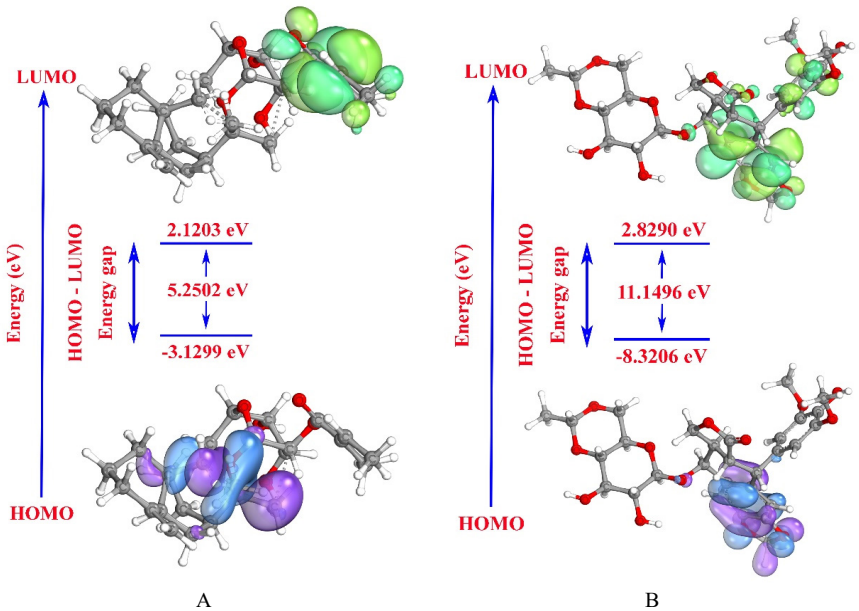

Figure 4. HOMO and LUMO surface diagrams of (A) CPD2 and (B) Etoposide.

the steric and electrostatic features of the Mcl-1 binding groove, consistent with the lower RMSD, Rg, and SASA values observed during MD simulations. This electronic adaptability may be advantageous for sustaining productive interactions with Mcl-1, thereby further supporting CPD2 as a promising computational hit for subsequent anti-gastric-cancer investigation.

4. CONCLUSIONS

Computational modelling assessed CPD2 as an Mcl-1 (6QFQ)-oriented candidate, using Etoposide as the reference ligand. Docking ranked CPD2 as the strongest binder among the tested sesquiterpene glycosides (-10.75 kcal/mol), exceeding Etoposide (-9.80 kcal/mol), with key contacts centered on Phe228, Met231, Val249, Met250, Val253, Leu267, and Phe270 and hydrogen-bond assignment to Arg263 and Leu267. Over 100 ns of molecular dynamics, the CPD2-6QFQ complex maintained a tighter conformational envelope, reflected in lower RMSD clustering (0.11-0.15 nm) and reduced, more stable Rg (1.42-1.44 nm) and SASA (82-88 nm^2). In contrast, Etoposide showed higher deviation and solvent exposure but more frequent hydrogen-bond events. MM/GBSA supported favorable association for both ligands, with closely comparable totals (ΔTOTAL = -28.72 ± 4.45 kcal/mol for CPD2; -29.80 ± 10.53 kcal/mol for Etoposide); CPD2 was driven primarily by van der Waals stabilization (ΔVDWAALS = -34.96 ± 4.29 kcal/mol) with a modest solvation penalty (ΔGSOLV = 8.63 ± 4.93 kcal/mol). At the same time, Etoposide combined stronger gas-phase terms with a larger polar desolvation cost (ΔEGB = 37.27 ± 8.14 kcal/mol). ADMET prediction indicated high intestinal absorption for CPD2 (94.482%) despite low solubility (-5.034 log mol/L), and DFT suggested predicted higher electronic polarizability for CPD2 (EHOMO = -3.1299 eV; ΔE = 5.2502 eV; ω = 0.0485 eV) relative to Etoposide (EHOMO = -8.3206 eV; ΔE = 11.1496 eV; ω = 0.6762 eV). Overall, convergence across docking, molecular dynamics, MM/GBSA, ADMET estimation, and DFT descriptors supports CPD2 as the leading in silico candidate, warranting lead-optimization efforts and experimental confirmation.

Taken together, these findings support CPD2 as a prioritized in silico hit for gastric cancer research through potential modulation of the anti-apoptotic protein Mcl-1. Nevertheless, in silico outputs represent prioritization evidence rather than biological proof, and experimental confirmation remains necessary to establish quantitative binding and functional impact. The present work did not incorporate in vitro or in vivo assays, limiting translational interpretation of predicted affinity, stability, and pharmacokinetic liabilities. Future studies should therefore implement biochemical binding measurements, gastric cancer cell-based assays, cellular models relevant to Mcl-1-dependent phenotypes, and pharmacokinetic testing to clarify exposure constraints suggested by the solubility-permeability balance and transporter-related predictions. Additional refinement via extended sampling and entropy-aware free-energy methods may further resolve the close energetic differences observed between CPD2 and the reference ligand.

5. ETHICAL STATEMENT

This work does not include any studies involving human or animal subjects.

6. CONFLICT OF INTEREST

The author declares no conflict of interest.

7. FUNDING

No funding was received to conduct this research.

8. AUTHORSHIP CONTRIBUTION STATEMENT

Hung Duc Nguyen: The author was solely responsible for the conception of the study, interpretation of the results, and preparation of the manuscript. All data were generated in-house, and no paper mill was used. All results were interpreted solely by the author; Grammarly and Google Translate were used for English language refinement.

9. REFERENCES

1. F. Bray, M. Laversanne, H. Sung, J. Ferlay, R.L. Siegel, I. Soerjomataram, and A. Jemal. Global cancer statistics 2022: GLOBOCAN estimates of incidence and mortality worldwide for 36 cancers in 185 countries. *CA: A Cancer Journal for Clinicians* 74(3): 229-263 (2024). DOI: 10.3322/caac.21834
2. Q. Luo and D.P. Smith. Global cancer burden: progress, projections, and challenges. *The Lancet* 406(10512): 1536-1537 (2025). DOI: 10.1016/S0140-6736(25)01570-3
3. T.I. Mamun, S. Younus, and M.H. Rahman.

Gastric cancer-epidemiology, modifiable and non-modifiable risk factors, challenges and opportunities: An updated review. *Cancer Treatment and Research Communications* 41: 100845 (2024). DOI: 10.1016/j.ctarc.2024.100845

4. H. Kumagai, S. Baba, H. Nikai, R. Fujisawa, M. Shimooki, and A. Sasaki. Stage IV gastric cancer with microsatellite instability-high achieving long-term survival by gastrectomy after nivolumab as third-line therapy: A case report and literature review. *Surgical Case Reports* 10(1): 221 (2024). DOI: 10.1186/s40792-024-02022-5
5. Y. Semenova, A. Kerimkulov, T. Uskenbayev, D. Zharlyganova, O. Shatkovskaya, T. Sarina, A. Manatova, G. Yessenbayeva, and T. Adylkhanov. Chemotherapy options for locally advanced gastric cancer: A review. *Cancers* 17(5): 809 (2025). DOI: 10.3390/cancers17050809
6. H.I. Akbarali, K.H. Muchhala, D.K. Jessup, and S. Cheatham. Chemotherapy induced gastrointestinal toxicities. In: Strategies to mitigate the toxicity of cancer therapeutics. D. A. Gewirtz and P. B. Fisher (Eds.). *Academic Press, Boston, USA* pp. 131-166 (2022). DOI: 10.1016/bs.acr.2022.02.007
7. H. Akagi, H. Higuchi, H. Sumimoto, T. Igarashi, A. Kabashima, H. Mizuguchi, M. Izumiya, G. Sakai, M. Adachi, S. Funakoshi, S. Nakamura, Y. Hamamoto, T. Kanai, H. Takaishi, Y. Kawakami, and T. Hibi. Suppression of myeloid cell leukemia-1 (Mcl-1) enhances chemotherapy-associated apoptosis in gastric cancer cells. *Gastric Cancer* 16(1): 100-110 (2012). DOI: 10.1007/s10120-012-0153-6
8. L.P. Zhang, Y.M. Wei, M.J. Luo, S.Y. Ren, X.W. Zhan, C. Wang, Z.F. Li, R.M. Zhu, S. Yan, Y. Cheng, J.L. Xu, X.J. Yang, K.L. Du, J.Q. Wang, G. Zhang, D.X. Du, R. Gao, D.B. Zhao, and J.N. Gong. Both direct and indirect suppression of MCL1 synergizes with BCLXL inhibition in preclinical models of gastric cancer. *Cell Death & Disease* 16(1): 170 (2025). DOI: 10.1038/s41419-025-07481-8
9. W. Likui, L. Qun, Z. Wanqing, S. Haifeng, L. Fangqiu, and L. Xiaojun. Prognostic role of myeloid cell leukemia-1 protein (Mcl-1) expression in human gastric cancer. *Journal of Surgical Oncology* 100(5): 396-400 (2009). DOI: 10.1002/jso.21344
10. F. Muller, C. Cerella, F. Radogna, M. Dicato, and M. Diederich. Effects of natural products on Mcl-1 expression and function. *Current Medicinal Chemistry* 22(30): 3447-3461 (2015). DOI: 10.2174/0929867322666150716115435
11. S.Y. Kang, D. Hwang, S. Shin, J. Park, M. Kim, M.D.H. Rahman, M.A. Rahman, S.G. Ko, and B. Kim. Potential of bioactive food components against gastric cancer: insights into molecular mechanism and therapeutic targets. *Cancers* 13(18): 4502 (2021). DOI: 10.3390/cancers13184502
12. Y. Jasoria, M. Agrawal, S. Kumar, H. Chaudhary, K.K. Sahu, M. Singhal, S. Arora, P. Chandolia, S. Saha, K. Singh, S. Mahour, W. Akram, and D. Jain. In-vivo evaluation of neuroprotective effect of Chinese plant *Calendula officinalis* Linn. flower extract against aluminium chloride-induced alzheimer's in wistar rats. *Pharmacological Research - Modern Chinese Medicine* 12: 100458 (2024). DOI: 10.1016/j.prmcm.2024.100458
13. M. D'Ambrosio, A. Ciocarlan, E. Colombo, A. Guerriero, C. Pizza, E. Sangiovanni, and M. Dell'Agli. Structure and cytotoxic activity of sesquiterpene glycoside esters from *Calendula officinalis* L.: Studies on the conformation of viridiflorol. *Phytochemistry* 117: 1-9 (2015). DOI: 10.1016/j.phytochem.2015.05.005
14. J.B. Murray, J. Davidson, I. Chen, B. Davis, P. Dokurno, C.J. Graham, R. Harris, A. Jordan, N. Matassova, C. Pedder, and S. Ray. Establishing drug discovery and identification of hit series for the anti-apoptotic proteins, Bcl-2 and Mcl-1. *ACS Omega* 4(5): 8892-8906 (2019). DOI:10.1021/acsomega.9b00611
15. D.V.D. Spoel, E. Lindahl, B. Hess, G. Groenhof, A.E. Mark, and H.J.C. Berendsen. GROMACS: Fast, flexible, and free. *Journal of Computational Chemistry* 26(16): 1701-1718 (2005). DOI: 10.1002/jcc.20291
16. N. Guex and M.C. Peitsch. SWISS-MODEL and the Swiss-Pdb Viewer: An environment for comparative protein modeling. *ELECTROPHORESIS* 18(15): 2714-2723 (1997). DOI: 10.1002/elps.1150181505
17. V. Zoete, M.A. Cuendet, A. Grosdidier, and O. Michielin. SwissParam: A fast force field generation tool for small organic molecules. *Journal of Computational Chemistry* 32(11): 2359-2368 (2011). DOI: 10.1002/jcc.21816
18. E.F. Pettersen, T.D. Goddard, C.C. Huang, G.S. Couch, D.M. Greenblatt, E.C. Meng, and T.E. Ferrin. UCSF Chimera-A visualization system for exploratory research and analysis. *Journal of Computational Chemistry* 25(13): 1605-1612 (2004). DOI: 10.1002/jcc.20084
19. H.D. Nguyen. Unveiling the anti-apoptotic mechanism of magnolialide as a colorectal cancer inhibitor via molecular modeling, ADMET, and MMGBSA analysis. *Physical Chemistry Research* 13(4): 783-796 (2025). DOI: 10.22036/

pcr.2025.535946.2708

20. D.E. Pires, T.L. Blundell, and D.B. Ascher. pkCSM: Predicting small-molecule pharmacokinetic and toxicity properties using graph-based signatures. *Journal of Medicinal Chemistry* 58(9): 4066-4072 (2015). DOI: 10.1021/acs.jmedchem.5b00104
21. F. Neese. Software update: The ORCA program system-version 6.0. *WIREs Computational Molecular Science* 15(2): e70019 (2025). DOI: 10.1002/wcms.70019
22. G. Knizia and J.E. Klein. Electron flow in reaction mechanisms-revealed from first principles. *Angewandte Chemie International Edition* 54(18): 5518-5522 (2015). DOI: 10.1002/anie.201410637
23. M.D. Hanwell, D.E. Curtis, D.C. Lonie, T. Vandermeersch, E. Zurek, and G.R. Hutchison. Avogadro: an advanced semantic chemical editor, visualization, and analysis platform. *Journal of Cheminformatics* 4(1): 17 (2012). DOI: 10.1186/1758-2946-4-17
24. A. Tiwari and S. Singh. Computational approaches in drug designing. In: Bioinformatics. D.B. Singh and R.K. Pathak (Eds.). *Academic Press, Boston, USA* pp. 207-217 (2022). DOI: 10.1016/B978-0-323-89775-4.00010-9
25. G.G. Ferenczy and M. Kellermayer. Contribution of hydrophobic interactions to protein mechanical stability. *Computational and Structural Biotechnology Journal* 20: 1946-1956 (2022). DOI: 10.1016/j.csbj.2022.04.025
26. L. Wang, Y. Chen, M. Zhang, J. Liu, H. Li, M. Liu, S. Wu, Y. Zhang, W. Li, and B. Wang. Chemical dissection of selective myeloid leukemia-1 inhibitors: How they were found and evolved. *European Journal of Medicinal Chemistry* 283: 117168 (2025). DOI: 10.1016/j.ejmech.2024.117168
27. F. Molani and A.E. Cho. Accurate protein-ligand binding free energy estimation using QM/MM on multi-conformers predicted from classical mining minima. *Communications Chemistry* 7(1): 247 (2024). DOI: 10.1038/s42004-024-01328-7
28. Q. Sun. The hydrophobic effects: Our current understanding. *Molecules* 27(20): 7009 (2022). DOI: 10.3390/molecules27207009
29. M.F. Adasme, K.L. Linnemann, S.N. Bolz, F. Kaiser, S. Salentin, V.J. Haupt, and M. Schroeder. PLIP 2021: Expanding the scope of the protein–ligand interaction profiler to DNA and RNA. *Nucleic Acids Research* 49(W1): W530-W534 (2021). DOI: 10.1093/nar/gkab294
30. M. Bello and C. Bandala. Evaluating the ability of end-point methods to predict the binding affinity tendency of protein kinase inhibitors. *RSC Advances* 13(36): 25118-25128 (2023). DOI: 10.1039/D3RA04916G
31. H. Uludağ and T. Tang, How can molecular dynamics simulations assist with gene medicines? *Biomaterials and Biosystems* 2: 100014 (2021). DOI: 10.1016/j.bbiosy.2021.100014
32. Z. Jin and Z. Wei. Molecular simulation for food protein–ligand interactions: A comprehensive review on principles, current applications, and emerging trends. *Comprehensive Reviews in Food Science and Food Safety* 23(1): e13280 (2024). DOI: 10.1111/1541-4337.13280
33. I.J. dos S. Nascimento, J.N.S. Gomes, J. de O. Viana, Y.M.S. de M. e Silva, E.G. Barbosa, and R.O. de Moura. The power of molecular dynamics simulations and their applications to discover cysteine protease inhibitors. *Mini Reviews in Medicinal Chemistry* 24(11): 1125-1146 (2024). DOI: 10.2174/1389557523666230901152257
34. S. Wang, X. Sun, W. Cui, and S. Yuan. MM/PB(GB)SA benchmarks on soluble proteins and membrane proteins. *Frontiers in Pharmacology* 13: 1018351 (2022). DOI: 10.3389/fphar.2022.1018351
35. E. Akkus, O. Tayfuroglu, M. Yildiz, and A. Kocak. Revisiting MMPBSA by adoption of MC-based surface area/volume, ani-ml potentials, and two-valued interior dielectric constant. *The Journal of Physical Chemistry B* 127(20): 4415-4429 (2023). DOI: 10.1021/acs.jpcb.3c00834
36. M. Taylor and J. Ho. MM/GBSA prediction of relative binding affinities of carbonic anhydrase inhibitors: effect of atomic charges and comparison with Autodock4Zn. *Journal of Computer-Aided Molecular Design* 37(4): 167-182 (2023). DOI: 10.1007/s10822-023-00499-0
37. R. Ancuceanu, B.E. Lascu, D. Drăgănescu, and M. Dinu. In silico ADME methods used in the evaluation of natural products. *Pharmaceutics* 17(8): 1002 (2025). DOI: 10.3390/pharmaceutics17081002
38. C.L. Pires and M.J. Moreno. Improving the accuracy of permeability data to gain predictive power: assessing sources of variability in assays using cell monolayers. *Membranes* 14(7): 157 (2024). DOI: 10.3390/membranes14070157
39. E.T.C. Huang, J.S. Yang, K.Y.K. Liao, W.C.W. Tseng, C.K. Lee, M. Gill, C. Compas, S. See, and F.J. Tsai. Predicting blood–brain barrier permeability of molecules with a large language model and machine learning. *Scientific Reports* 14(1): 15844 (2024). DOI: 10.1038/s41598-024-66897-y
40. Y. Zhang, Z. Wang, Y. Wang, W. Jin, Z. Zhang, L.

Jin, J. Qian, and L. Zheng. CYP3A4 and CYP3A5: the crucial roles in clinical drug metabolism and the significant implications of genetic polymorphisms. *PeerJ* 12: e18636 (2024). DOI: 10.7717/peerj.18636

41. S. Asano, A. Galetin, Y. Tomita, K.M. Giacomini, X. Chu, X. Yang, T. Nakamura, H. Kusuhara, and Y. Sugiyama, Predicting OCT2/MATEs-mediated drug interactions in healthy volunteers and patients with chronic kidney disease: insights from extended clearance concept, endogenous biomarkers, and in vitro inhibition studies (perspectives from the international transpor. *Clinical Pharmacology & Therapeutics* 118(5): 994-1014 (2025). DOI: 10.1002/cpt.3727
42. G. Falcón-Cano, A. Morales-Helguera, H. Lambert, M.Á. Cabrera-Pérez, and C. Molina. hERG toxicity prediction in early drug discovery using extreme gradient boosting and isometric stratified ensemble mapping. *Scientific Reports* 15(1): 15585 (2025). DOI: 10.1038/s41598-025-99766-3
43. N. Cerisier, E. Truong, T. Watanabe, T. Oshiro, T. Takahashi, S. Ito, and O. Taboureau. Computational prediction of mutagenicity through comprehensive cell painting analysis. *Mutagenesis* 40(4): 560-574 (2025). DOI: 10.1093/mutage/geaf014
44. P. Geerlings. From density functional theory to conceptual density functional theory and biosystems. *Pharmaceuticals* 15(9): 1112 (2022). DOI: 10.3390/ph15091112
45. M. Franco-Pérez, F. Heidar-Zadeh, P.W. Ayers, F. De Proft, A. Vela, J.L. Gázquez, and P. Geerlings. Temperature and external fields in conceptual density functional theory. *Chemical Science* 15(48): 20090-20121 (2024). DOI: 10.1039/D4SC04181J
46. S.R. Pilli, T. Banerjee, and K. Mohanty. HOMO–LUMO energy interactions between endocrine disrupting chemicals and ionic liquids using the density functional theory: Evaluation and comparison. *Journal of Molecular Liquids* 207: 112-124 (2015). DOI: 10.1016/j.molliq.2015.03.019
47. P. Pérez, L.R. Domingo, A. Aizman, and R. Contreras. The electrophilicity index in organic chemistry. In: Theoretical aspects of chemical reactivity. Chapter 19. A. Toro-Labbé (Ed.). *Elsevier, Amsterdam, Netherlands* pp. 139-201 (2007) DOI: 10.1016/S1380-7323(07)80010-0